Optimizing Interface Conductivity in Electronics
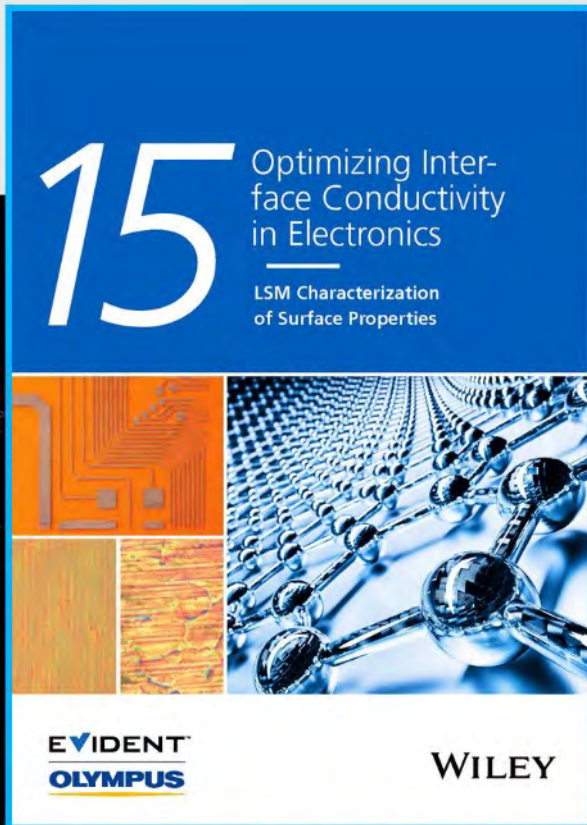
The latest eBook from Advanced Optical Metrology. Download for free.

15 Optimizing Interface Conductivity in Electronics

LSM Characterization of Surface Properties

EVIDENT OLYMPUS

WILEY

Surface roughness is a key parameter for judging the performance of a given material's surface quality for its electronic application. A powerful tool to measure surface roughness is 3D laser scanning confocal microscopy (LSM), which will allow you to assess roughness and compare production and finishing methods, and improve these methods based on mathematical models.

Focus on creating high-conductivity electronic devices with minimal power loss using laser scanning microscopy is an effective tool to discern a variety of roughness parameters.

EVIDENT OLYMPUS

WILEY

4D Printing Auxetic Metamaterials with Tunable, Programmable, and Reconfigurable Mechanical Properties

Xiaozhou Xin, Liwu Liu,* Yanju Liu, and Jinsong Leng*

Auxetic mechanical metamaterials, which expand transversely when axially stretched, are widely used in flexible electronics and aerospace. However, these chiral metamaterials suffer from three severe limitations as a typical auxetic metamaterials: narrow strain range, non-tunable mechanical behaviors, and fixed properties after fabrication. In this work, 4D printing chiral metamaterials with tunable, programmable, and reconfigurable properties are developed. The deformation mode transforms from bending dominated to stretching dominated under large deformation, leading to the stress–deformation (σ–λ) behavior of the auxetic metamaterials similar to those of the biomaterials ("J"-shaped), such as tissues or organs. The programmability and reconfigurability of the developed chiral metamaterials allow mechanical behavior to change between different biomaterials with high precision. Furthermore, scaffolds with personalized mechanical properties as well as configurations and meta-materials-based light-emitting diode integrated devices demonstrate potential applications in tissue engineering and programmable flexible electronics.

1. Introduction

Metamaterials are any engineering materials composed of unique microstructures when arranged in an orderly manner, and can exhibit attractive properties not found in natural materials.[1–4] The emergence of these metamaterials makes it possible to customize the macroscopic physical properties (i.e., mechanical, acoustic, thermal, electromagnetic, etc.) by designing the topological parameters and arrangement of the microstructures.[5] Auxetic mechanical metamaterial (negative Poisson's ratio metamaterial) expands transversely when subjected to axial stretching,[6–8] and exhibits excellent mechanical properties such as shear resistance,[9–11] indentation resistance,[12–14] and negative thermal expansion.[15–18] The extraordinary properties enable the auxetic mechanical meta-materials to contribute to the development of advanced functional materials and their immense application prospects.[18–22]

X. Xin, Prof. L. Liu, Prof. Y. Liu
Department of Astronautical Science and Mechanics
Harbin Institute of Technology (HIT)
P.O. Box 301, No. 92 West Dazhi Street, Harbin 150001, P. R. China
E-mail: liulw@hit.edu.cn, liuliwu_006@163.com
Prof. J. Leng
Center for Composite Materials and Structures
Harbin Institute of Technology (HIT)
P.O. Box 3011, No. 2 Yikuang Street, Harbin 150080, P. R. China
E-mail: lengjs@hit.edu.cn

The ORCID identification number(s) for the author(s) of this article can be found under https://doi.org/10.1002/adfm.202004226.

DOI: 10.1002/adfm.202004226

However, conventional chiral metamaterial, as a branch of auxetic metamaterial, is limited in the range of strain (less than a few percent), and the negative Poisson's ratio behavior independent of geometric parameters.[7,23] The geometric diversity of the wavy ligament microstructure provides a wide range of tunable mechanical properties for metamaterials. Due to bionic mechanical properties, such as adjustable Poisson's ratio, "J"-shaped stress–strain relationship and large deformation, meta-materials composed of wavy microstructures have shown promising application prospects in flexible electronics and tissue engineering.[25] Previous study reported that the artificial skin composed of zigzag microstructure was able to match the nonlinear mechanical behavior of cat's skin.[19]

3D printing technology overcomes the long-standing obstacles that traditional manufacturing processes cannot use highly ordered material architectures in 3D space to achieve complex design concepts.[5] Some mechanical metamaterials with complex microstructures, such as lattice structures[23–29] and hierarchical architected metamaterials,[30] have been successfully prepared by 3D printing. The mechanical properties of metamaterials depend on the configuration and spatial arrangement of the microstructures, which means that the properties are fixed and irreversible after fabrication.[5] 4D printing, a combination of 3D printing and stimulus-responsive materials, makes these properties reversible.[31–33] The printed object can adaptively change its configuration/property by the external stimuli (i.e., thermal, magnetic, electrical, etc.). Shape memory polymer (SMP), as a type of stimulus-responsive material, possesses the ability to maintain a temporary shape and recover to its original shape under the environmental stimuli.[34–36] Recently, based on the variable stiffness and shape memory effect (SME), SMP-based metamaterials with energy absorption, mode conversion, reconfigurability, tunability, and programmability characteristics have been developed.[5,37–40]

In this work, the chiral metamaterials with large deformation, programmable, reconfigurable, and tunable properties were developed by 4D printing. The arc-shaped and crescent-shaped ligament microstructures were introduced into the chiral metamaterials to solve the limitations of narrow strain range and non-tunable mechanical behaviors of conventional chiral metamaterials. The scalable manufacturing of the structures was accomplished by constraining the center coordinates of the nodes. The effects of geometric topological parameters and deformation (λ) on the mechanical properties of metamaterials (Poisson's

**ADVANCED
SCIENCE NEWS**

www.advancedsciencenews.com

**ADVANCED
FUNCTIONAL
MATERIALS**

www.afm-journal.de

ratio, σ–λ behavior) under infinitesimal and large deformation were investigated. The quantitative relationship between mechanical properties and λ achieved the programmability and reconfigurability of the metamaterial, breaking through the limitation that the properties of conventional chiral metamaterials cannot be changed once manufactured. The diversity of the microstructure provided tunable mechanical properties in a wider range, demonstrating a great degree of design freedom. More interestingly, the developed metamaterials were able to simulate the "*J*"-shaped σ–λ curves of specific tissues/organs, and can convert to another biomaterial through programming. Finally, the potential applications of chiral metamaterials in flexible electronics and tissue engineering were demonstrated by programmable light-emitting diode (LED) integrated device and customized scaffold. Different from the existing customized scaffolds, the scaffolds proposed in this work can be customized in terms of configurations and mechanical properties of the tissue. Compared with previous works on the structures with wavy ligaments, the developed metamaterials increased the geometric parameters to increase the design freedom.[19,38,40] The mechanical properties of the metamaterials exhibited a wide range of tunable domains, allowing the σ–λ curves to reproduce a variety of biomaterials.

2. Design and Fabrication of Auxetic Materials

The microstructure of four types of developed chiral materials has a 180° rotational symmetry (**Figure 1**), consisting of wavy filamentous ligaments and nodes (cylinders). The chiral metamaterial can be divided into hexa- (Figure 1a,b) and tetra-chiral metamaterial (Figure 1c,d) depending on the number of ligaments surrounding each node. The array spacing of ligaments around the node of the unit cell of the hexa- and tetra-chiral metamaterial is $\pi/3$ and $\pi/2$, respectively. According to the geometric configuration of the ligament, it can be divided into arc-shaped ligament (Figure 1a,c) and crescent-shaped ligament (Figure 1b,d).

The six dimensionless geometric parameters of the microstructure, including ω/l_1, l_2/l_1, R_0/l_1, t_2/l_1, t_1/l_1, and 2θ (2α), determine the macroscopic configuration and mechanical properties of the metamaterials (Figure 1). ω is the thickness, l_1 is the distance between two adjacent nodes, l_2 is the distance between two ends of the ligament, R_0 is the outer diameter of the node, t_1 and t_2 are the widths of ligament and node as well as 2θ and 2α are the central angle of arc-shaped and crescent-shaped ligament, respectively.

A series of metamaterials with different geometric parameters were designed. The node coordinates of all microstructures were constrained to enable the metamaterials to be fabricated in a scalable manner. The CAD models of the auxetic materials with different geometric parameters can be observed in Figure 1e, Figure S1 and Table S1 (Supporting Information). In this work, the influence of geometric parameters R_0/l_1 (0.129, 0.193, 0.258), and 2θ (2α) ($\pi/6$, $\pi/3$, $\pi/2$, $2\pi/3$, $5\pi/6$, π) on the effective mechanical properties of the metamaterials was investigated. By default, $\omega/l_1 = 0.097$, $l_2/l_1 = 0.966$, $t_2/l_1 = 0.064$, and $t_1/l_1 = 0.032$.

A high-precision additive manufacturing technology-laser cladding deposition (LCD) 3D printer was employed to fabricate SMP auxetic metamaterials, as shown in **Figure 2**a. The sliced
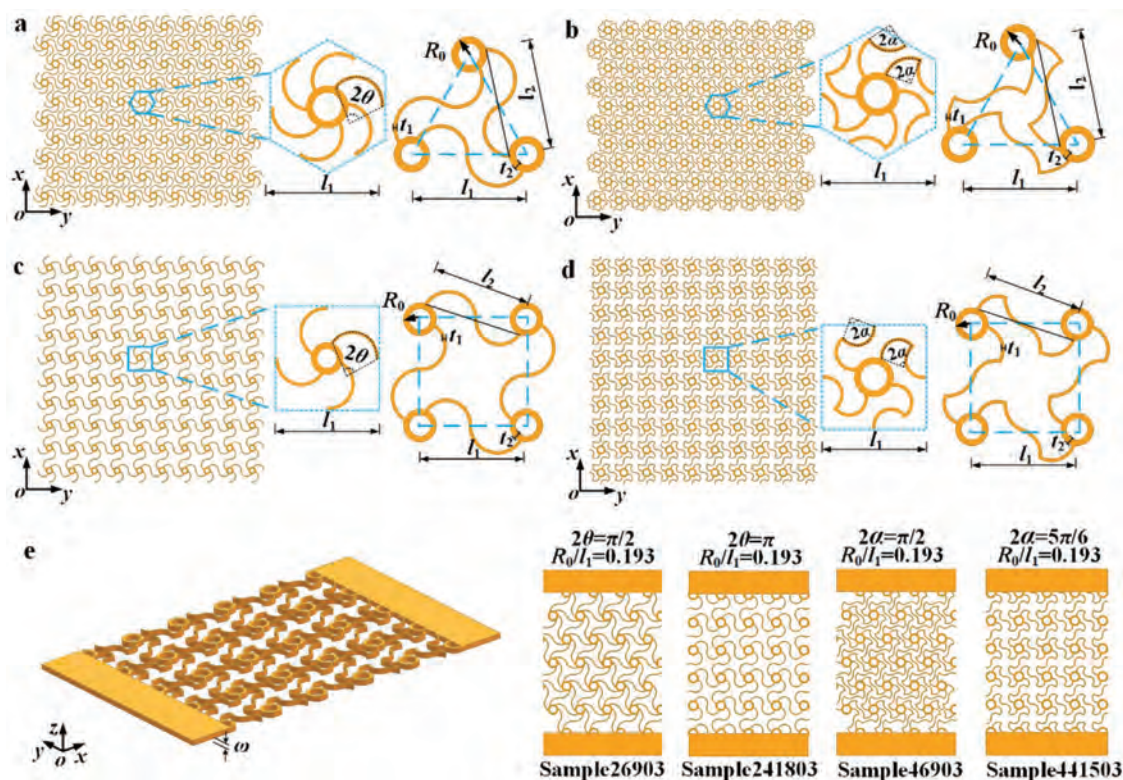

Figure 1. CAD models and geometric parameters of the auxetic metamaterials. Hexa-chiral metamaterial with a) arc-shaped ligament and b) crescent-shaped ligament. Tetra-chiral metamaterial with c) arc-shaped ligament and d) crescent-shaped ligament. e) Printed models of metamaterials.
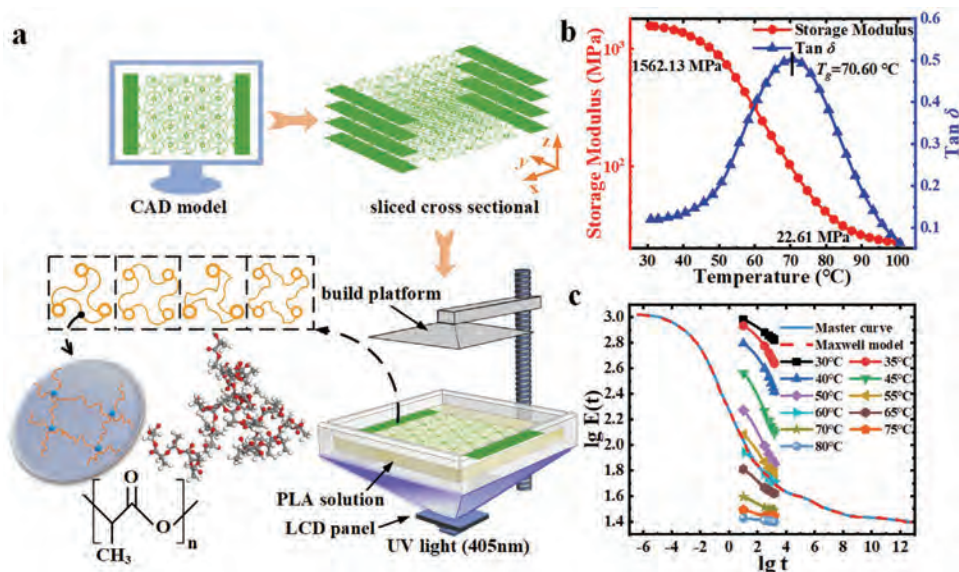
**ADVANCED
SCIENCE NEWS**
www.advancedsciencenews.com

**ADVANCED
FUNCTIONAL
MATERIALS**
www.afm-journal.de

Figure 2. 4D printing of mechanical metamaterials: a) printing process and the molecular structure of PLA-based SMP, b) DMA test curves, c) relaxation modulus of SMP at different temperatures, comparison of experimental and theoretical model calculation results of the master curve at T_{ref} = 60 °C.

cross-sectional images were generated by the slicing software (ANYCUBIC Photon Slicer). LCD masking technology, with the used of an LCD panel to adjust the UV light, selectively transmitted the UV light with a wavelength of 405 nm generated from the LED. The metamaterial was printed layer by layer using photopolymerized the precursor solution. As shown in Figure S2 (Supporting Information), the printed mechanical metamaterials showed favorable printing quality, which was further verified by SEM (Figure S3, Supporting Information).

The photocurable polylactic acid (PLA)-based SMP precursor solution formed a physical cross-linking network with the soft segment (switch phase) and the hard segment (permanent phase) after photopolymerization. The soft segments were movable and random molecular chains. The hard segments were the physical cross-linking points that determine the recovery performance of SMP. The programming process of auxetic metamaterials was as follows: (i) Heating: when the metamaterial was subjected to external tensile load and the temperature was higher than its glass transition temperature (T_g), the random molecular chains (soft segments) of SMP were stretched and the center angle of the metamaterial ligament was changed from 2θ (2α) to $2\theta'$ ($2\alpha'$). (ii) Cooling: the orientation of molecular chains was fixed and the internal stress was frozen after holding the load and cooling the metamaterial to room temperature. (iii) Unloading: the metamaterial was fixed in this temporary shape after unloading. The central angle of the ligament was changed from $2\theta'$ ($2\alpha'$) to $2\theta''$ ($2\alpha''$) due to elastic recovery. (iv) Reheating: when reheated ($>T_g$), the molecular chains recovered to the random state, which caused the metamaterial to recover to its original shape, the central angle of the ligament was changed from $2\theta''$ ($2\alpha''$) to 2θ (2α).

The dynamic mechanical analysis (DMA) of the printed sample showed that the T_g of SMP was 70.60 °C (Figure 2b). The isothermal (25 °C) quasi-static uniaxial tensile test of the printed SMP standard sample showed that Young's modulus, strength, and elongation were ≈1.4 GPa, 48 MPa, and 9%,

respectively (Figure S4a, Supporting Information). The time- and temperature-dependent properties of the relaxation modulus are shown in Figure 2c and Figure S4 (Supporting Information). The multi-branch constitutive model was applied to describe the viscoelastic behavior of SMP, which reproduced the master curve (T_{ref} = 60 °C) with high accuracy (see Section S2, Supporting Information for details).

3. Negative Poisson's Ratio Behavior under Infinitesimal Deformation

The prediction model of tetra-/hexa-chiral metamaterial with arbitrary ligament shape was derived to investigate the influence of geometric parameters on the effective mechanical properties (see Section S3, Supporting Information for details). The Cartesian coordinate system $o'\text{-}x'y'$ was established to describe the central axis of ligament with arbitrary shape. The origin of coordinate o' was set at the joint of ligament and node (**Figure 3**a). The free-body diagram of the tetra- and the hexa-chiral metamaterial cell are shown in Figure 3b,c. 2θ and 2α were replaced by 2β to describe ligaments of arbitrary shape, i.e., the geometric parameters were ω/l_1, l_2/l_1, R_0/l_1, t_2/l_1, t_1/l_1, and 2β. β was the angle between the end of the ligament and x' axis. β of the arc-shaped and the crescent-shaped ligaments were θ and $\pi/4\text{-}\alpha$, respectively. The nodes were assumed as rigid bodies, and Euler–Bernoulli beam was used to simulate the deformation behavior of ligaments due to the slender configuration of ligaments.[19,25]

Considering membrane energy and bending energy, the total strain energy of the cell with arbitrary ligament shape is

$$U_{all} = \frac{1}{2EA}\int_0^{s_{end}}\left(\sum_{i=1}^n N_i^2\right)ds + \frac{1}{2EI}\int_0^{s_{end}}\left(\sum_{i=1}^n M_i^2\right)ds \tag{1}$$

where E is the elastic modulus of SMP, A is the cross-sectional area of the ligament ($A = \omega t_1$), I is the second moment of the
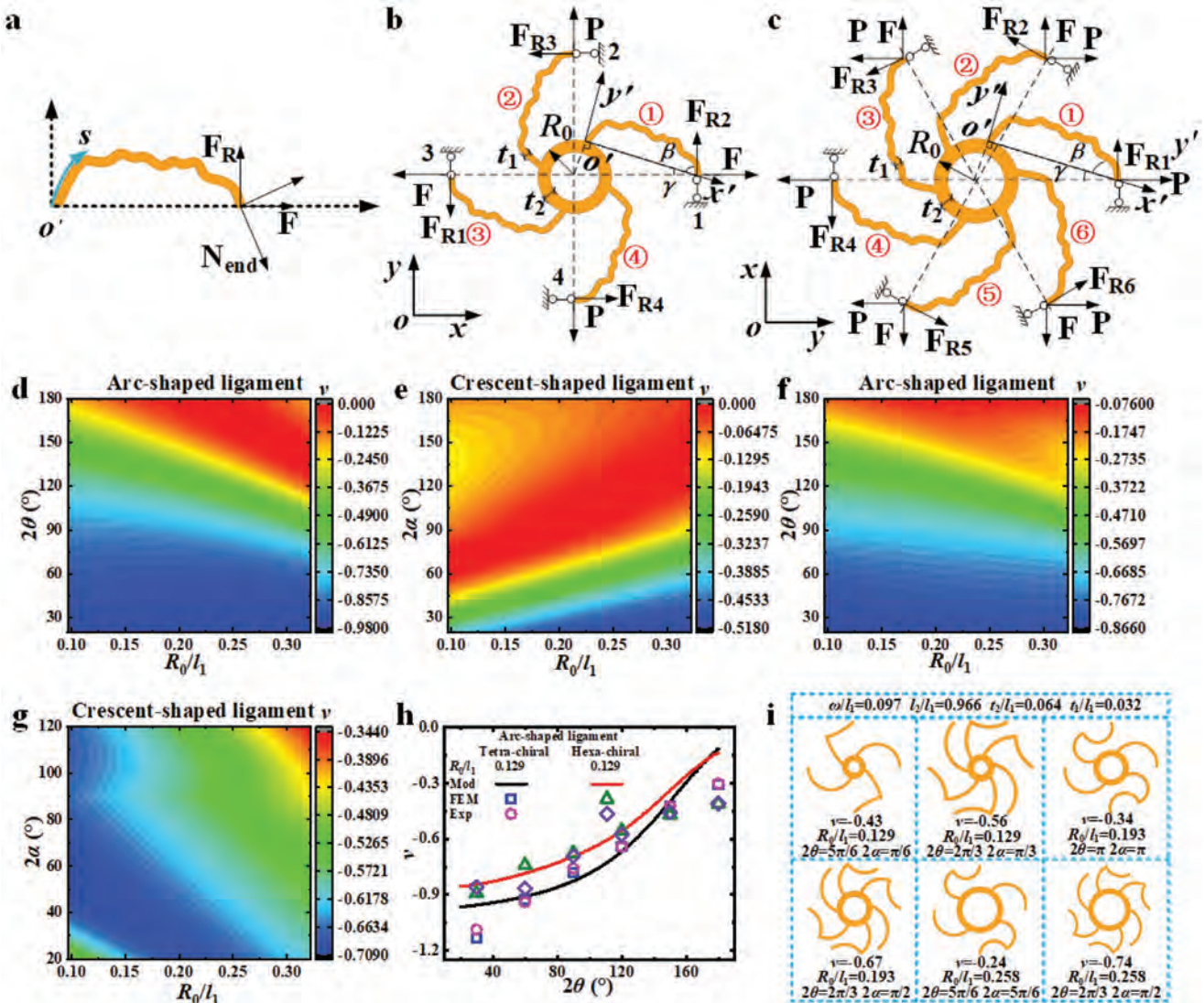
Figure 3. a) The arbitrary shape ligament in local coordinate system o'-$x'y'$. The free-body diagram of b) tetra-chiral and c) hexa-chiral metamaterial cell. Theoretical study on the influence of geometric parameters of ligament and node on Poisson's ratio under infinitesimal deformation. Tetra-chiral metamaterials with d) arc-shaped ligament, e) crescent-shaped ligament. Hexa-chiral metamaterials with f) arc-shaped ligament, g) crescent-shaped ligament. The tunability and designability of the metamaterials under infinitesimal deformation: h) comparison of model prediction, finite element analysis and experiment of Poisson's ratio of the metamaterials. i) The combination of cells with similar Poisson's ratio can increase design freedom.

ligament ($I = \omega t_1^3 / 12$), n is the number of ligaments, and S_{end} is the total arc length of the ligament.

The average strain in the x direction of tetra-chiral metamaterial can be obtained by Castigliano's theorem, i.e.

$$
\begin{aligned}
\varepsilon_x &= \frac{\delta_x}{l_1} \\
&= \frac{F}{EAl_1} \left[2(\beta_1 + \beta_4) + 4\zeta_1^2 (\beta_2 + \beta_3) + 4\zeta_1 (\beta_5 - \beta_6 - \beta_7 + \beta_8) \right. \\
&\quad + \left. (4 - 8\zeta_1^2)\beta_9 \right] + \frac{F}{EIl_1} \left[2(\beta_{11} + \beta_{12}) + 4\zeta_1^2 (\beta_{10} + \beta_{13}) \right. \\
&\quad + \left. 4\zeta_1 (\beta_{15} - \beta_{14} - \beta_{17} + \beta_{16}) + (8\zeta_1^2 - 4)\beta_{18} \right]
\end{aligned}
\tag{2}
$$

Similarly, the ε_y can be obtained by

$$
\begin{aligned}
\varepsilon_y &= \frac{\left. \frac{\partial U_{all}}{\partial P} \right|_{P=0}}{l_1} = \frac{F}{EAl_1} \left[-2\zeta_1 (\beta_5 - \beta_6 - \beta_7 + \beta_8) \right] \\
&\quad + \frac{F}{EIl_1} \left[-2\zeta_1 (\beta_{15} - \beta_{14} - \beta_{17} + \beta_{16}) \right]
\end{aligned}
\tag{3}
$$

The effective Poisson's ratio (ν_{eff}) of the tetra-chiral metamaterial is

$$
\nu_{eff} = -\frac{\varepsilon_y}{\varepsilon_x} = -\frac{HI + BA}{CI + DA}
\tag{4}
$$

**ADVANCED
SCIENCE NEWS**

www.advancedsciencenews.com

**ADVANCED
FUNCTIONAL
MATERIALS**

www.afm-journal.de

where $H = -2\zeta_1(\beta_5 - \beta_6 - \beta_7 + \beta_8)$, $B = -2\zeta_1(\beta_{15} - \beta_{14} - \beta_{17} + \beta_{16})$, $C = 2(\beta_1 + \beta_4) + 4\zeta_1^2(\beta_2 + \beta_3) + 4\zeta_1(\beta_5 - \beta_6 - \beta_7 + \beta_8) + (4 - 8\zeta_1^2)\beta_9$, $D = 2(\beta_{11} + \beta_{12}) + 4\zeta_1^2(\beta_{10} + \beta_{13}) + 4\zeta_1(\beta_{15} - \beta_{14} - \beta_{17} + \beta_{16}) + (8\zeta_1^2 - 4)\beta_{18}$.

Similarly, the effective Poisson's ratio (ν_{eff}) of the hexa-chiral metamaterial is

$$
\begin{aligned}
\nu_{eff} &= -\frac{\varepsilon_y}{\varepsilon_x} \\
&= -\frac{2\sqrt{3}}{3} \frac{A_y + \zeta_1 B_y + \zeta_4 C_y + \zeta_5 D_y}{A_x + \zeta_1 B_x + \zeta_1^2 C_x + \zeta_4 D_x + \zeta_4^2 E_x + \zeta_5 F_x + \zeta_5^2 I_x + \zeta_1\zeta_4 G_x + \zeta_1\zeta_5 H_x + \zeta_4\zeta_5 M_x}
\end{aligned}
\tag{5}
$$

The influence of the geometric parameters of the ligament (2θ and 2α) and node (R_0/l_1) on the Poisson's ratio of chiral structures were examined according to the theoretical model, as shown in Figure 3d–g. The Poisson's ratio of the auxetic materials achieved tunability by changing geometric parameters. The nodes rotated and the ligaments connected to the nodes expanded laterally with the application of σ (Figure S7, Supporting Information). When the geometric parameters of the metamaterials with arc-shaped and crescent-shaped ligament were the same, the S_{end} of metamaterial with crescent-shaped ligament was longer. The β_i of the metamaterial was associated with the central axis expression of ligament configuration. Therefore, the difference of U_{all} led to the difference of Poisson's ratio tunable domain of the metamaterial with arc-shaped and crescent-shaped ligament. Figure 3d,e exhibit contour plots of the effect of geometric parameters on the Poisson's ratio of the tetra-chiral metamaterials with arc-shaped and crescent-shaped ligament, respectively. The arc-shaped ligament exhibited a wider Poisson's ratio tunable domain (–0.98 to 0), while the crescent-shaped ligament had a narrower Poisson's ratio domain of –0.5 to 0. The auxetic behavior of the structure gradually weakened with the increase of 2θ (2α). Besides, when $\pi/9 \leq 2\theta \leq \pi/2$, the tunable domain of the Poisson's ratio of the structure was –0.98 to –0.8, in which the Poisson's ratio was insensitive to R_0/l_1. When $2\theta > \pi/2$, Poisson's ratio was sensitive to the geometric parameters of ligament and node. The crescent-shaped ligament of the cell contained two arcs, which led to a smaller Poisson's ratio than the arc-shaped when $\pi/9 \leq 2\alpha \leq \pi/2$. This also resulted in a narrower Poisson's ratio tunable domain in the chiral structure with crescent-shaped ligaments. The adjustable domain of Poisson's ratio of arc-shaped and crescent-shaped hexa-chiral metamaterials were –0.86 to –0.08 and –0.71 to –0.34, respectively (Figure 3f,g). The influence of the geometric parameters of ligament and node on the hexa-chiral metamaterials with arc-shaped ligament was similar to that of the tetra-chiral metamaterials.

The analytical solution, finite element analysis, and experimental results of Poisson's ratio for chiral structures with different geometric parameters are shown in Figure 3h. The analytical solutions were generally higher than the experimental value, which might be caused by the fact that the deformation of the node and the shear deformation of the beam were neglected in the total energy of the cell.

The above analysis has shown that the macroscopic mechanical properties of the metamaterials can be designed by adjusting the geometric parameters of the microstructures. In fact, there are many solutions to design the required

Poisson's ratio. Two or more cells with similar Poisson's ratio can be selected to form a new configuration. For example, Figure 3i shows the unit cell pattern of the combined structure of $\nu = -0.43$, –0.56, –0.34, –0.67, –0.24, and –0.74. The combination of multiple microstructures with similar Poisson's ratio increased the design freedom, which was useful for adjusting other effective mechanical properties (e.g., stiffness and nonlinear deformation behavior) of the metamaterials.

4. Nonlinear Behavior of Auxetic Materials under Large Deformation

The mechanical behaviors of the auxetic metamaterial were strongly dependent on the geometric parameters of the microstructure. When subjected to tensile loads, the original curved ligaments arranged compactly were gradually straightened. Therefore, the metamaterial experienced nonlinear deformation. **Figure 4** shows the experimental and simulated results of the samples under different λ. It can be observed that the tangent direction of the ligaments was gradually parallel to the load direction with the increase of λ. Before the curved ligament was stretched to be flat, bending deformation was the dominant deformation mode. After that, the metamaterial entered the stretching-dominated deformation mode. The transformation of the deformation mode resulted in the "J"-shaped σ–λ curve of the metamaterial (**Figure 5**a,d,g,j). When the material was in the bending-dominated deformation mode, the σ–λ curve exhibited a relatively constant stress plateau region, that was, the stress remained constant as λ increased. In this deformation mode, the second moment of the sectional area determined the effective stiffness. When the deformation of the metamaterial exceeded critical deformation (λ_{cr}), the deformation mode of the metamaterial was stretching-dominated. The cross-sectional area determined the effective stiffness in this deformation mode, which resulted in the effective stiffness of the metamaterial increased sharply compared to the bending-dominated deformation mode. This phenomenon was more obvious when the ligament had a larger curvature. This meant that the modulus of the metamaterial in the bending-dominated deformation mode was lower than that in the stretching-dominated deformation mode.

The effective stiffness of the metamaterial decreased as 2θ (2α) increased, as shown in Figure 5a,d,g,j. The λ_{cr} of the metamaterial decreased with the decrease of 2θ (2α), which led to the higher modulus of the metamaterial with smaller central angle. Therefore, the effective stiffness was the highest among the tested specimens when 2θ (2α) = 30°, and the stiffness decreased with the increase of the curvature of the ligament. The stiffness of the crescent-shaped ligament was lower than that of arc-shaped ligament, which was caused by the configuration of ligaments. The cell with crescent-shaped ligament
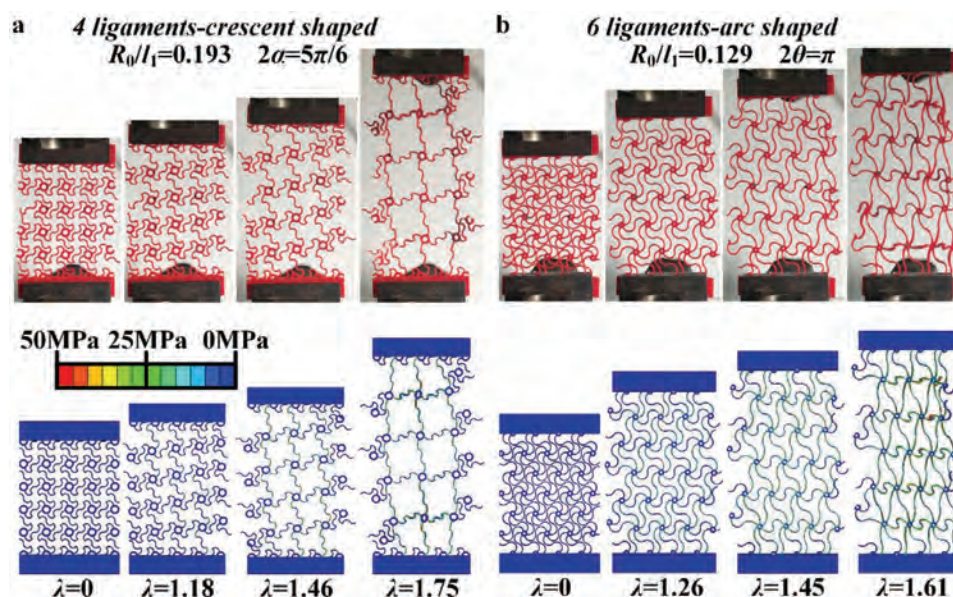
**ADVANCED
SCIENCE NEWS**
www.advancedsciencenews.com

**ADVANCED
FUNCTIONAL
MATERIALS**
www.afm-journal.de

Figure 4. Comparison of experimental optical images and FEM results under different λ a) sample 441503, b) sample 261802.

contained two arcs, while arc-shaped ligament contained only one segment (i.e., S_{end}). When the geometric parameters of the two types of ligaments were the same, the λ_{cr} of arc-shaped ligament was lower than that of crescent-shaped ligament, which led to the higher effective modulus of metamaterials with arc-shaped ligament. Interestingly, the elongation of the PLA-based SMP was ≈9%, and the maximum deformation of the metamaterial was ≈90% (changed ≈10 times). In addition to stretchability, metamaterials also exhibited softness and elasticity at room temperature (Movie S1, Supporting Information).

Figure 5 and Figures S8 and S9 (Supporting Information) reveal the FEM and experimental results of the influence of λ and geometric parameters on the Poisson's ratio of the material. The FEM results were in complete agreement with the experimental results. In the bending-dominated deformation mode, the deformation of the ligament caused the nodes connected with the ligament to rotate (Figure S7, Supporting Information). The rotating nodes stretched the ligament perpendicular to the loading direction, which caused the metamaterial to exhibit auxetic behavior at the macroscopic level. The metamaterial entered the stretching-dominated deformation mode with the increase of λ. The ligament, which was perpendicular to the loading direction, contracted and produced out-of-plane deformation, resulting in the weakened auxetic behavior and even a positive Poisson's ratio. Obviously, the geometric parameters determined the rotation angle of the node and λ_{cr} of the two deformation modes. λ_{cr} increased with the increase of ligament curvature. $\lambda_{cr} = ≈1.15$, when $2\theta = 60°$; but $\lambda_{cr} = ≈1.55$ when the angle was increased to 180°. For the tetra-chiral metamaterials, the auxetic behavior of the metamaterial was more obvious with the increase of λ in the region of bending-dominated deformation mode. The hexa-chiral metamaterial exhibited a relatively constant negative Poisson's ratio. Figure 5 and Figure S9 (Supporting Information) exhibit the Poisson's ratio versus λ for metamaterials with different geometric parameters. The

continuous variation of ν provided an opportunity for the programmability of the metamaterials.

The auxetic materials can be programmed with different configurations due to SME. Movie S1 (Supporting Information) demonstrates the shape memory programming process for metamaterials including shape programming and shape recovery. First, the material was placed in hot water (≈90 °C) and stretched to the programmed deformation λ_{target}. Then the new configuration can be fixed after cooling and unloading. The programmed shape can be used as a new kind of auxetic materials to realize the programmability of their mechanical properties. That was, the unique characteristic was attributed to SME and the changes in ligament geometric parameters (from 2θ (2α) to $2\theta''$ ($2\alpha''$)). The configuration and mechanical properties of the metamaterial recovered to its original state after reheating, demonstrating the reconfigurability of the metamaterial.

As shown in **Figure 6**a, the σ–λ curve of the metamaterial can be converted into other metamaterials' curves by programming. For example, when $\lambda_{target} = 1.2$, the σ–λ behavior of the samples 241204, 46603, and 441503 were similar to those of 24902, 46303, and 44603, respectively. Figure 6b reveals the programmability of Poisson's ratio. When $\lambda_{target} = 1.2$ and 1.3, the Poisson's ratio of sample 261503 was similar to that of sample 26902 and sample 26302, respectively.

5. Implications

The developed metamaterials exhibited negative Poisson's ratio and "J"-shaped σ–λ curves, enabling their promising potential applications in the field of biomaterials. It was worth noting that the developed metamaterial was able to replicate the nonlinear mechanical responses of specific tissues and organs within the optimal deformation range ($\lambda \in [1, 1.45]$) (**Figure 7**a–c), such as pig belly skin, iliac artery, muscle fiber, and dog lung (data from

**ADVANCED
SCIENCE NEWS**

www.advancedsciencenews.com

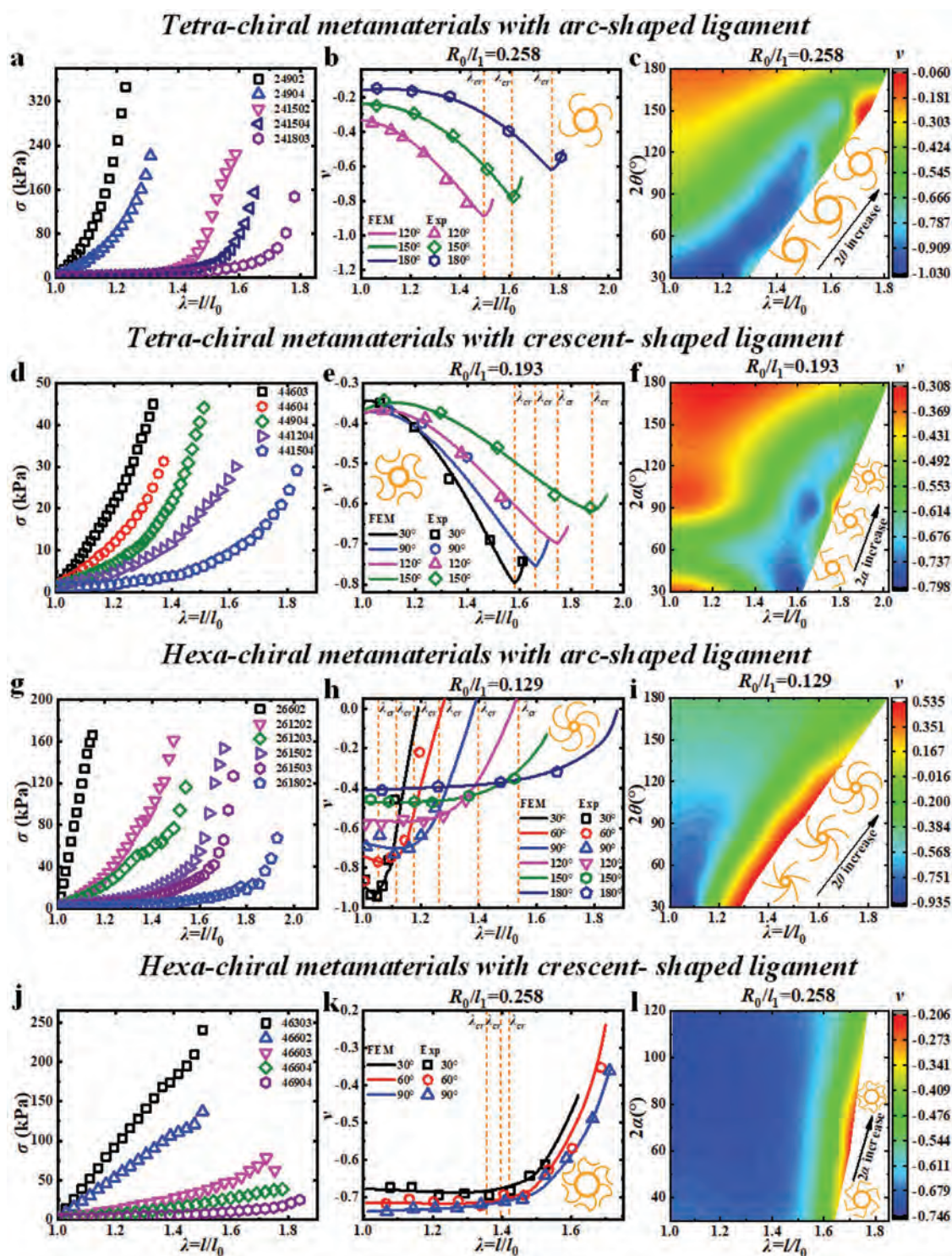**ADVANCED
FUNCTIONAL
MATERIALS**

www.afm-journal.de

Figure 5. Nonlinear mechanical behavior of the metamaterials under large deformation. Tetra-chiral metamaterials with arc-shaped ligament ($R_0/l_1 = 0.258$): a) σ–λ test curves. b) Comparison of FEM and experimental results of ν under different λ. c) Contour plot of FEM results of the effect of 2θ on Poisson's ratio. Tetra-chiral metamaterials with crescent-shaped ligament ($R_0/l_1 = 0.193$): d) σ–λ test curves. e) Comparison of FEM and experimental results of ν under different λ. f) Contour plot of FEM results of the effect of 2α on Poisson's ratio. Hexa-chiral metamaterials with arc-shaped ligament ($R_0/l_1 = 0.129$): g) σ–λ test curves. h) Comparison of FEM and experimental results of ν under different λ. i) Contour plot of FEM results of the effect of 2θ on Poisson's ratio. Hexa-chiral metamaterials with crescent-shaped ligament ($R_0/l_1 = 0.258$): j) σ–λ test curves. k) Comparison of FEM and experimental results of ν under different λ. l) Contour plot of FEM results of the effect of 2α on Poisson's ratio.

ADVANCED
SCIENCE NEWS
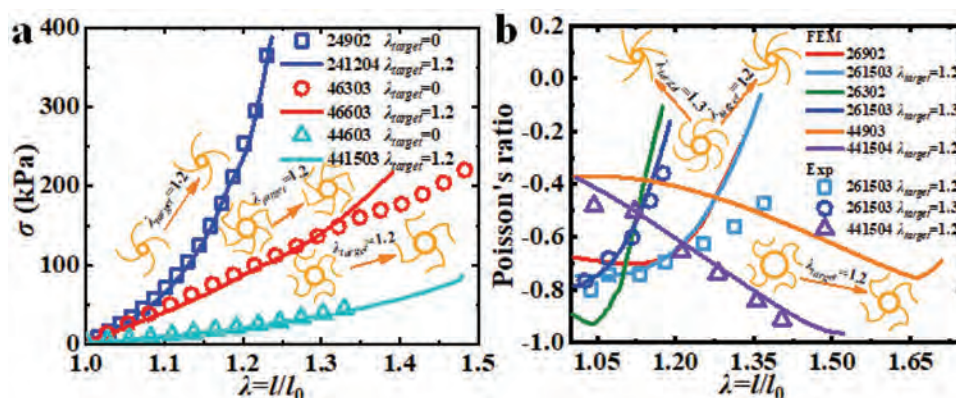www.advancedsciencenews.com

ADVANCED
FUNCTIONAL
MATERIALS
www.afm-journal.de

Figure 6. The tunability and programmability of the mechanical properties of chiral metamaterials: a) the nonlinear relationship of σ–λ and b) the Poisson's ratio behavior.

ref. [41]). In addition, the nonlinear deformation behavior of the metamaterials enabled the conversion of between two different biomaterials through programming (Figure 7d). The nonlinear σ–λ response of sample 44903 before and after programming was similar to the iliac artery and lens capsules, respectively, which demonstrated the programmable mechanical properties of the metamaterial.

The application potential of metamaterials in the field of flexible electronics cannot be ignored. **Figure 8** exhibits a programmable and stretchable LED device, consisting of a pig belly-like metamaterial, Ag and three in series LEDs. The external DC power (8.5 V) was used to power the device. Movie S2

(Supporting Information) shows the optical images of the device stretched in different directions. The device also can be programmed to different configurations by shape memory programming. During the stretching and programming process, the brightness of the LED and the system current remained almost unchanged. In addition, as shown in Figure 8 and Movie S2 (Supporting Information), the LED integrated device fitted the skin, and the brightness of the LED was generally unchanged under slow and rapid breathing. LEDs can be replaced by other inorganic electronic components or commercial chips to enrich the functions of the devices, for example, for health monitoring.
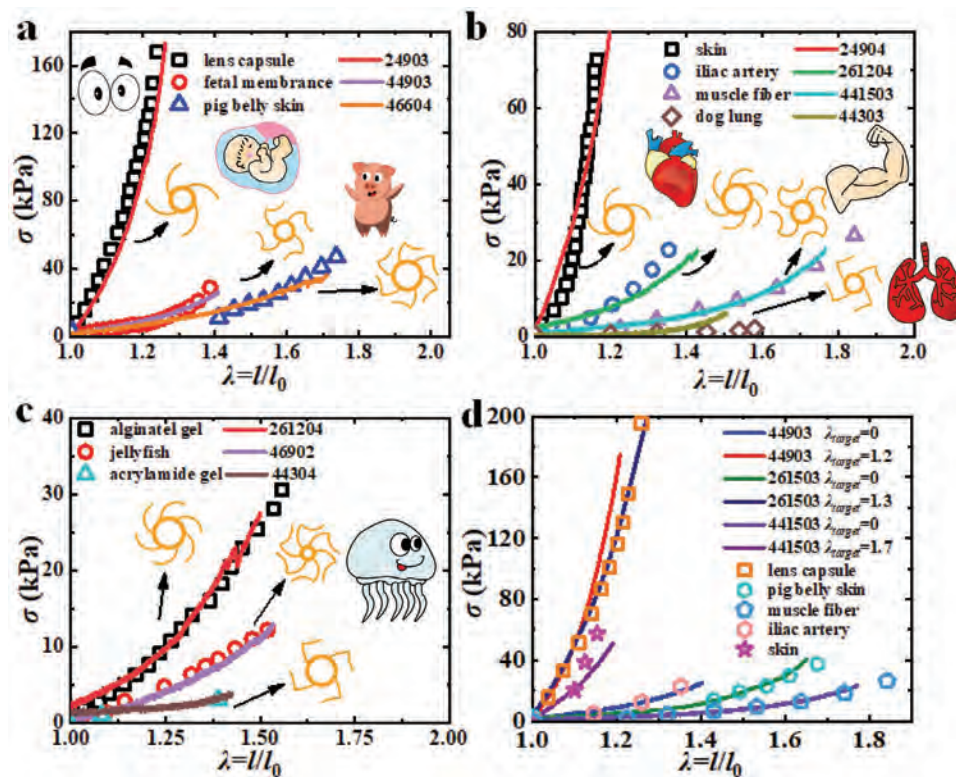

Figure 7. a–c) Comparison of σ–λ curves between metamaterials and tissues/organs.[41] d) Metamaterials enable the conversion between two biomaterials through programming.
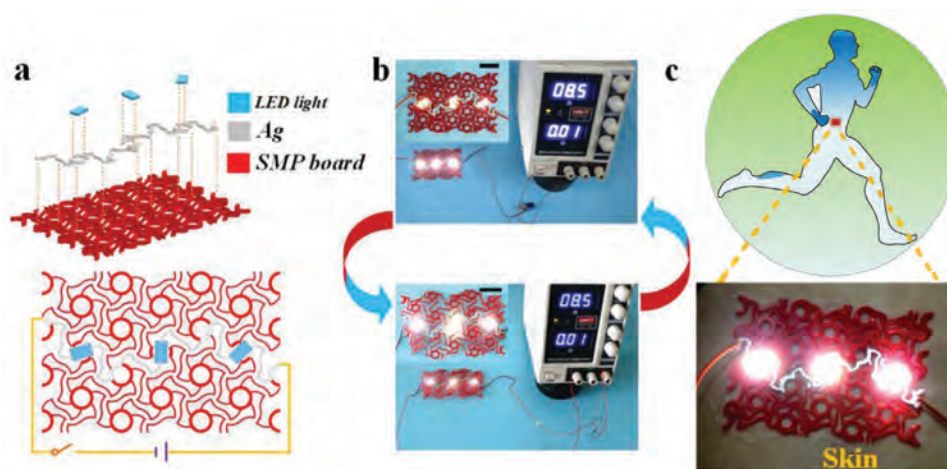
Figure 8. Application of metamaterials in LED integrated devices: a) exploded views and circuit diagram of the device, b) the optical image of the device before and after programming, c) the device fitted the skin. The scale bar is 20 mm.

The σ–λ curve of sample 261204 was similar to that of the iliac artery, showing the potential of metamaterials as a biomedical scaffold. **Figure 9** demonstrates the cylindrical shell derived from sample 261204. The cylindrical shell was magnified twice, because the auxetic behavior of the metamaterial was not affected by the scale (Figure S10, Supporting Information). The scaffold can deform together with the blood vessels because of their similar mechanical behaviors. Due to the tunability of mechanical properties and 4D printing technology, the scaffold can match the blood vessel in terms of mechanical properties

and geometry. Additionally, Figure 9, Figure S11 and Movie S3 (Supporting Information) show the programming ability of cylindrical shell in different deformation modes of compression, torsion and stretch–torsion coupling, demonstrating the feasibility of metamaterials to construct 3D complex structures.

6. Conclusion

In summary, novel programmable and tunable chiral metamaterials were designed and fabricated by 4D printing. The deformation mode of the metamaterial transformed from bending-dominant mode to stretching-dominated mode with the increase of λ, which led to the auxetic behavior and the nonlinear "J"-shaped σ–λ behavior. It was worth noting that the maximum strain of the developed metamaterial was ≈90%, which was nearly 10 times larger than that of the raw material. The quantitative relationship between mechanical properties and deformation under large deformation provided opportunities for the programming of metamaterials. Programmable, tunable, and reconfigurable mechanical properties of the metamaterials were verified. More interestingly, the σ–λ behavior of the auxetic materials was able to match specific tissues/organs (i.e., pig belly skin, iliac artery, muscle fiber, and dog lung), and can transform between two biomaterials. LED integrated device demonstrated its potential application in flexible electronics. In addition, a negative Poisson's ratio shape memory biomedical scaffold with customized mechanical properties and configuration showed the possibility of the developed metamaterial expanding into 3D space.
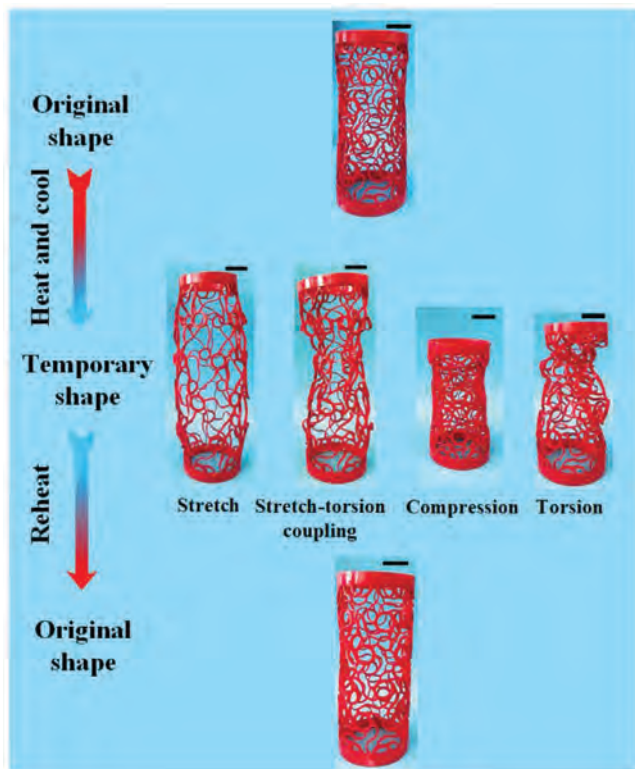
7. Experimental Section

Design and Fabrication of Auxetic Materials: Siemens PLM Software UG NX10.0 was employed to build the CAD models of mechanical metamaterial and then the models were sliced through the ANYCUBIC Photon Slicer64 software. The LCD 3D printer (ANYCUBIC Photon) was used to fabricate metamaterials. The LED wavelength, *XY*-axis resolution and *Z*-axis accuracy of the printer were 405 nm, 0.047 mm, and 0.00125 mm, respectively. The maximum volume of the printed sample

Figure 9. Shape memory programming process of the cylindrical shell. The scale bar is 30 mm.

was 115 mm (length) × 65 mm (width) × 155 mm (height). PLA-based photocurable liquid polymer (eSUN-PLA) purchased from eSUN was used as the photocurable SMP precursor solution. The exposure time for printing each layer was 10 s and the layer thickness was 0.05 mm.

Experimental Method: The printed PLA-based SMP sample (20 × 5 × 2 mm) was used to characterize the dynamic mechanical behavior on DMA Q800. The sample was heated from 30 to 100 °C at 3°C min^{-1}. The preload was 0.001 N, and the strain oscillated at 1 Hz.

According to the standard ASTM D638, the isothermal uniaxial tensile test (25 °C) was performed on the printed dumbbell-shaped sample (115 × 6 × 2 mm). The test was carried out on a Zwick-010 tensile tester equipped with an environmental chamber. Before the test, the sample was placed at the target temperature for 30 min. The sample was loaded at 2 mm min^{-1} until failure.

The stress relaxation behavior of PLA-based SMP at different temperatures (30, 35, 40, 45, 50, 55, 60, 65, 70, 75, and 80 °C) was examined one by one. Then, the sample was stretched and maintained this deformed state for 1800 s. During this process, the attenuation of the force was recorded.

The surface morphology of the printed samples was characterized by VEGA3 TESCAN SEM at an accelerating voltage of 20.0 kV.

The nonlinear behavior of the metamaterials was also investigated by Zwick-010 tensile tester at 2 mm min^{-1} tensile rate. Canon DS126571 was employed to record the optical images to calculate the Poisson's ratio.[18]

The demonstration of metamaterials based LED integrated devices has been given the informed written consent of the participant (the first author of the manuscript) and approved by the Ethics Research Committee of the School of Astronautics of Harbin Institute of Technology.

Finite Element Analysis: The commercial finite element software ABAQUS (3DS Dassault Systèmes, France) was employed to calculate the nonlinear deformation behavior of the metamaterial.

Supporting Information

Supporting Information is available from the Wiley Online Library or from the author.

Acknowledgements

Conflict of Interest

The authors declare no conflict of interest.

Keywords

[1] T. Frenzel, M. Kadic, M. Wegener, *Science* **2017**, *358*, 1072.
[2] K. Bertoldi, V. Vitelli, J. Christensen, M. van Hecke, *Nat. Rev. Mater.* **2017**, *2*, 17066.
[3] A. A. Zadpoor, *Mater. Horiz.* **2016**, *3*, 371.
[4] F. Pan, Y. L. Li, Z. Y. Li, J. L. Yang, B. Liu, Y. L. Chen, *Adv. Mater.* **2019**, *31*, 1900548.
[5] C. Yang, M. Boorugu, A. Dopp, J. Ren, R. Martin, D. Han, W. Choi, H. Lee, *Mater. Horiz.* **2019**, *6*, 1244.
[6] G. N. Greaves, A. L. Greer, R. S. Lakes, T. Rouxel, *Nat. Mater.* **2011**, *10*, 823.
[7] H. M. A. Kolken, A. A. Zadpoor, *RSC Adv.* **2017**, *7*, 5111.
[8] S. Babaee, J. Shim, J. C. Weaver, E. R. Chen, N. Patel, K. Bertoldi, *Adv. Mater.* **2013**, *25*, 5044.
[9] T. Buckmann, M. Thiel, M. Kadic, R. Schittny, M. Wegener, *Nat. Commun.* **2014**, *5*, 4130.
[10] J. B. Choi, R. S. Lakes, *J. Mater. Sci.* **1992**, *27*, 5375.
[11] J. B. Choi, R. S. Lakes, *J. Mater. Sci.* **1992**, *27*, 4678.
[12] K. E. Evans, A. Alderson, *Adv. Mater.* **2000**, *12*, 617.
[13] N. Chan, K. E. Evans, *J. Cell. Plast.* **1998**, *34*, 231.
[14] K. L. Alderson, A. Fitzgerald, K. E. Evans, *J. Mater. Sci.* **2000**, *35*, 4039.
[15] X. Ni, X. Guo, J. Li, Y. Huang, Y. Zhang, J. A. Rogers, *Adv. Mater.* **2019**, *31*, 1905405.
[16] L. L. Wu, B. Li, J. Zhou, *ACS Appl. Mater. Interfaces* **2016**, *8*, 17721.
[17] A. D. Fortes, E. Suard, K. S. Knight, *Science* **2011**, *331*, 742.
[18] H. Zhang, X. G. Guo, J. Wu, D. N. Fang, Y. H. Zhang, *Sci Adv* **2018**, *4*.
[19] J. Liu, Y. Zhang, *Soft Matter* **2018**, *14*, 693.
[20] A. Papadopoulou, J. Laucks, S. Tibbits, *Nat. Rev. Mater.* **2017**, *2*, 17078.
[21] O. Duncan, T. Shepherd, C. Moroney, L. Foster, P. Venkatraman, K. Winwood, T. Allen, A. Alderson, *Appl. Sci.* **2018**, *8*, 941.
[22] X. L. Yu, J. Zhou, H. Y. Liang, Z. Y. Jiang, L. L. Wu, *Prog. Mater. Sci.* **2018**, *94*, 114.
[23] A. Clausen, F. Wang, J. S. Jensen, O. Sigmund, J. A. Lewis, *Adv. Mater.* **2015**, *27*, 5523.
[24] J. Liu, Y. Zhang, *J. Appl. Mech.* **2018**, *85*, 051003.
[25] Q. Ma, H. Y. Cheng, K. I. Jang, H. W. Luan, K. C. Hwang, J. A. Rogers, Y. G. Huang, Y. H. Zhang, *J. Mech. Phys. Solids* **2016**, *90*, 179.
[26] Y. Chen, T. Li, F. Scarpa, L. Wang, *Phys. Rev. Appl.* **2017**, *7*, 024012.
[27] L. R. Meza, S. Das, J. R. Greer, *Science* **2014**, *345*, 1322.
[28] S. Q. Yuan, C. K. Chua, K. Zhou, *Adv. Mater. Technol.* **2019**, *4*, 1800419.
[29] R. Hedayati, S. J. Salami, Y. Li, M. Sadighi, A. A. Zadpoor, *Phys. Rev. Appl.* **2019**, *11*, 034057.
[30] L. R. Meza, A. J. Zelhofer, N. Clarke, A. J. Mateos, D. M. Kochmann, J. R. Greer, *Proc. Natl. Acad. Sci. U. S. A.* **2015**, *112*, 11502.
[31] X. Kuang, D. J. Roach, J. T. Wu, C. M. Hamel, Z. Ding, T. J. Wang, M. L. Dunn, H. J. Qi, *Adv. Funct. Mater.* **2019**, *29*, 1805290.
[32] A. S. Gladman, E. A. Matsumoto, R. G. Nuzzo, L. Mahadevan, J. A. Lewis, *Nat. Mater.* **2016**, *15*, 413.
[33] W. Zhao, L. W. Liu, F. H. Zhang, J. S. Leng, Y. J. Liu, *Mater. Sci. Eng., C* **2019**, *97*, 864.
[34] T. Mu, L. W. Liu, X. Lan, Y. J. Liu, J. S. Leng, *Compos. Sci. Technol.* **2018**, *160*, 169.
[35] J. S. Leng, X. Lan, Y. J. Liu, S. Y. Du, *Prog. Mater. Sci.* **2011**, *56*, 1077.
[36] C. Lin, J. X. Lv, Y. S. Li, F. H. Zhang, J. R. Li, Y. J. Liu, L. W. Liu, J. S. Leng, *Adv. Funct. Mater.* **2019**.
[37] C. Yuan, X. M. Mu, C. K. Dunn, J. Haidar, T. J. Wang, H. J. Qi, *Adv. Funct. Mater.* **2018**, *28*.
[38] M. Lei, W. Hong, Z. Zhao, C. Hamel, M. J. Chen, H. B. Lu, H. J. Qi, *ACS Appl. Mater. Interfaces* **2019**, *11*, 22768.
[39] Z. A. Zhao, C. Yuan, M. Lei, L. Yang, Q. Zhang, H. S. Chen, H. J. Qi, D. N. Fang, *Phys. Rev. Appl.* **2019**, *11*.
[40] D. Wang, H. P. Xu, J. Q. Wang, C. R. Jiang, X. Y. Zhu, Q. Ge, G. Y. Gu, *ACS Appl. Mater. Interfaces* **2020**, *12*, 22146.
[41] S. S. Sheiko, A. V. Dobrynin, *Macromolecules* **2019**, *52*, 7531.